SPACE WEATHER, VOL. 8, S07004, doi:10.1029/2009SW000531, 2010

Application of a new phenomenological coronal mass ejection model to space weather forecasting

T. A. Howard[1] and S. J. Tappin[2]

Received 15 October 2009; revised 27 April 2010; accepted 6 May 2010; published 24 July 2010.

[1] Recent work by the authors has produced a new phenomenological model for coronal mass ejections (CMEs). This model, called the Tappin-Howard (TH) Model, takes advantage of the breakdown of geometrical linearity when CMEs are observed by white-light imagers at large distances from the Sun. The model extracts 3-D structure and kinematic information on the CME using heliospheric image data. This can estimate arrival times of the CME at 1 AU and impact likelihood with the Earth. Hence the model can be used for space weather forecasting. We present a preliminary evaluation of this potential with three mock trial forecasts performed using the TH Model. These are already-studied events from 2003, 2004 and 2007 but we performed the trials assuming that they were observed for the first time. The earliest prediction was made 17 hours before impact and predicted arrival times reached differences within one hour for at least one forecast for all three events. The most accurate predicted arrival time was 15 min from the actual, and all three events reach accuracies of the order of 30 min. Arrival speeds were predicted to be very similar to the bulk plasma speed within the CME near 1 AU for each event, with the largest difference around 300 km/s and the least 40 km/s. The model showed great potential and we aspire to fully validate it for integration with existing tools for space weather forecasting.

Citation: Howard, T. A., and S. J. Tappin (2010), Application of a new phenomenological coronal mass ejection model to space weather forecasting, *Space Weather*, *8*, S07004, doi:10.1029/2009SW000531.

1. Introduction

[2] The most severe space weather effects, called (geo)magnetic storms have long been known to cause a number of deleterious technological effects at Earth. Such effects include spacecraft damage and orbit degradation, increase of radiation dosage to aircraft staff and passengers and astronauts, and damage to power lines and power stations. The importance of addressing the problems regarding space weather on Earth has been reported in a recent National Academies Workshop on the topic [*Baker et al.*, 2009].

[3] Severe space weather effects are caused by coronal mass ejections (CMEs) which are large eruptions of magnetic field and plasma from the Sun. They often contain masses in excess of 10^{13} kg and close to the Sun they may achieve speeds greater than 3000 km s^{-1}. Statistical studies of CMEs and their properties can be found in the work by *Hundhausen et al.* [1994], *St. Cyr et al.* [2000] and *Yashiro et al.* [2004]. CMEs are typically observed in white light using coronagraphs such as LASCO on board the SOHO spacecraft [*Brueckner et al.*, 1995] and with heliospheric imagers such as SMEI on board Coriolis [*Eyles et al.*, 2003] and the HIs on board STEREO [*Eyles et al.*, 2009].

[4] Upon their occasional impact with the Earth CMEs may compress the magnetosphere, allowing the cusp region to move equatorward and the polar caps to grow. If the magnetic orientation of a CME is southward, magnetic reconnection allows the injection of large concentrations of energetic particles into the magnetosphere, which may result in an intensification of the ring current [*Dungey*, 1963]. The two most important properties governing space weather are hence the ram pressure exerted on the magnetosphere by the CME (which is related to its speed and density) and the orientation of its magnetic field.

[5] Contemporary efforts regarding such space weather forecasting are based on models that impose the physics of CME evolution on an erupting structure, often using near-Sun empirical data such as coronagraph CME properties, solar flares or CME-related radio bursts. Evolutionary physics imposed on CMEs varies from aerodynamics [*Cargill*, 2004; *Tappin*, 2006] to shock mechanics [*Hakamada*

[1]Department of Space Studies, Southwest Research Institute, Boulder, Colorado, USA.
[2]National Solar Observatory, Sunspot, New Mexico, USA.

Table 1. Assumptions That Can Be Applied to CMEs When They Are at Various Distances From the Sun[a]

Elongation (approx.)	Assumption	Reference
$\varepsilon < 15°$	Point P + small $\angle$	
$15 \le \varepsilon \le 30°$	Point P	*Houminer and Hewish* [1972]
$30 \le \varepsilon \le 45°$	Fixed Phi	*Kahler and Webb* [2007]
$\varepsilon > 45°$	TH Model	*Howard and Tappin* [2009a]

[a]Distances here are measured in units of elongation ε where 0° indicates the location of the Sun and 90° is the observer plane. These are accompanied by an appropriate reference.

and Akasofu, 1982; *Fry et al.*, 2001] to ejecta inclusion [*Chen*, 1996; *Odstrcil et al.*, 2003].

2. Improving Prediction Times

[6] *Webb et al.* [2009] present a summary of the accuracies of various CME Earth arrival time prediction techniques including those using some of the physical evolution models (their Section 4.2.1). The most accurate predicted arrival time cited was ±11 hours from the ISPM magnetohydrodynamic model [*Smith and Dryer*, 1995]. Recent years have seen little progress in improving CME arrival time prediction accuracy.

[7] One reason for this lack of progress could be that CME evolution models couple two separate problems associated with CME measurement.

[8] 1. The physics describing the appearance of the CME;

[9] 2. The physics describing the evolution of the CME.

[10] The former is governed by the geometry and the laws of Thomson scattering by which white light CMEs are observed. The latter applies predetermined assumptions of CME evolution through the heliosphere and then modifies boundary conditions (often in an ad hoc fashion) to fit new data sets as they become available. The coupling of these two problems means that if either of the assumptions are incorrect or inaccurate, then an inaccurate prediction of CME trajectory can easily result. This may arise from the boundary conditions obtained from secondary phenomena (such as solar flares or radio bursts) or parameters derived from sky plane projected images of CMEs. Further inaccuracies appear if the physical assumptions for evolution are incorrect or lacking. Hence it seems reasonable to state that if the two problems can be decoupled then more accurate descriptions of CME trajectory may result. In other words, if the CME structure and kinematics could be described using only the physics describing its appearance, then these parameters could be derived from the data alone without the need to apply the physics describing its evolution. The result could lead to (among other things) more accurate CME impact probability, speed and arrival time forecasting.

[11] It is not possible to extract three-dimensional (3-D) properties from single-viewpoint white light images alone when observing close to the Sun (within around 15° elongation). This is because the geometry and Thomson scattering physics near the Sun impose linearity. So the assumptions we can apply to simplify geometrical measurements of coronagraph CMEs near the Sun also restrict our ability to extract 3-D information. When white light CMEs are observed at farther distances from the Sun such as with heliospheric imagers, the linearity assumption breaks down and a more complex treatment needs to be applied in order to consider the effects of geometry and Thomson scattering. While the analysis becomes more complex, the advantage is that 3-D information becomes available in white light images of CMEs at large distances that is not available when they are close to the Sun. Hence it is possible to extract 3-D kinematic and structural properties of a CME using white light images alone, provided the CME is a large distance from the Sun. Table 1 shows the assumptions that can be applied for CMEs at various elongations.

[12] The utility of heliospheric image data to investigate space weather and estimate CME arrival time at the Earth was first attempted by *Howard et al.* [2006b], using SMEI data. They predicted the arrival times of a number of CMEs at the Earth and compared them with the actual arrival times of the associated interplanetary shocks at ACE. The difference between predicted and actual arrival times was on average around 11.5 hours, but the difference was within 2 hours for two events. *Webb et al.* [2006] discussed the geoeffectiveness of Earth-directed CMEs and found that of the 14 geomagnetic storms, 10 were associated with SMEI CMEs, with first detection just under 30 hours before the storm on average. Another study reported in the same paper revealed 39 out of 46 SMEI event related storms with first detection within 2 days prior to storm onset. *Webb et al.* [2009] studied some 14 geoeffective CMEs using SMEI and found predicted arrival times with accuracies around 10.5 hours (RMS) which was found to be marginally more accurate than any of the other compared prediction methods. Geoeffective CMEs have also been studied using the Heliospheric Imagers (HIs) on board STEREO. Such studies include *Harrison et al.* [2008] and *Davis et al.* [2009] but to the authors' knowledge no space weather survey involving STEREO CMEs has yet been published.

[13] The studies discussed in the previous paragraph show that heliospheric image data alone can be used to predict CME arrival times with accuracies better than current space weather forecasting models, but at the cost of later detection and forecast time. Those studies were conducted with relatively simple assumptions of CME structure and trajectory, with Point P assuming a basic spherical arc and Fixed-Phi assuming a single-point CME. *Lugaz et al.* [2009] present a comparison of the two techniques for a single event observed in January 2007. It seems likely that a more complex application of the physics responsible for the appearance of the CME will lead to more accurate predictions of arrival time at the Earth.

[14] This paper reports on a preliminary study involving the application of a newly developed phenomenological CME model for space weather forecasting. This new

technique, called the TH Model, combines the physics of Thomson scattering at large distances with geometry to reconstruct the structure and trajectory of CMEs using heliospheric image data alone. We have staged three mock forecasts on previously studied geoeffective CMEs in order to ascertain its potential speed and accuracy. We find great potential for the utility of this model and justify further validation for space weather forecasting.

3. TH Model

[15] The Tappin-Howard (TH) Model is a phenomenological CME reconstruction tool based on leading edge measurements from white light heliospheric images. It does not attempt to reproduce the density structure of the CME, only its leading edge. Other techniques exist that attempt density reconstruction, such as the tomographic model of Jackson [*Jackson and Froehling*, 1995; *Jackson et al.*, 2006], but these take a long time to perform and can not currently be used for space weather forecasting. The TH Model is a high-speed alternative to complete density reconstruction, based on the assumption that we only require the leading edge of the CME to gain a good estimate of the arrival time and speed at the Earth.

[16] The model works by comparing simulated leading edges for CMEs of various size, structure and propagation properties with actual leading edge measurements obtained directly from white light images. The development and application of the model have been discussed in a series of three papers in *Space Science Reviews*. The first part of the series [*Howard and Tappin*, 2009a] establishes the theoretical groundwork for the model while the second part [*Tappin and Howard*, 2009] discusses the model itself and its application to white light SMEI data. In the third and final part, *Howard and Tappin* [2009b] extend the model to accommodate STEREO data and apply it to an event observed by SMEI and STEREO. These papers discuss the first version of the model (hereafter referred to as Version 1) but an improved version (Version 2) has since been developed.

3.1. Version 1

[17] Version 1 began with two base structures that were modified to simulate the CMEs. These were a spherical bubble with one end at the Sun and the diameter aligned along the direction of propagation, and a spherical shell with the Sun as the center. *Lugaz et al.* [2009] apply the spherical bubble approach to CMEs observed with STEREO, while the spherical shell has previously been applied via the well-known "cone model" [*Xie et al.*, 2004]. Apparent leading edges for each structure can be determined by combining the physics of Thomson scattering with the geometry of the CME relative to a fixed observer, following the theory of *Howard and Tappin* [2009a].

[18] The basic structure is altered via a distortion parameter for the bubbles and latitude and longitude width parameters for the shell. The CME is then directed along a fixed trajectory and the resulting apparent leading edges for an observer at any location produced. Different parameters for structure and trajectory are then incrementally chosen and the observers selected as the Earth (SMEI) and the STEREO spacecraft. Hence a hypercube of simulated leading edges is produced with one edge for each combination of parameters. The hypercube contains several hundred thousand simulated leading edges.

[19] When a CME is observed in white light heliospheric images its leading edge can be measured for each heliospheric image in which it appears. The leading edges are currently measured manually by the user but developments are underway to automate this process. Regions of noise (data gaps) and the time at which the CME no longer appears are noted as these are also important parameters for the TH Model. This white light leading edge sequence is then compared with the simulated leading edges using a genetic algorithm followed by a simplex conversion. The result is the combination of parameters that best matches the measured leading edges, with error contours showing the "goodness" of each parameter conversion. From this parameter combination the 3-D structure of the CME can be reconstructed, along with its trajectory and speed of propagation.

[20] The model works in two stages. In Stage 1 the speed is a fixed parameter but it is allowed to vary in Stage 2, allowing a measurement of the distance evolution of the CME. The utility of Version 1 has been demonstrated by *Tappin and Howard* [2009] and *Howard and Tappin* [2009b], with very encouraging results.

3.2. Version 2

[21] Version 2 works on the same basic principle as Version 1, i.e. simulated leading edges are compared with actual leading edges resulting in a set of matching parameters, but the base structure of the CME has been altered. The two structures from Version 1 were combined to produce a single distorted shell base structure. So, where Version 1 worked with two hypercubes containing combinations of five (bubble) and six (shell) parameters, Version 2 contains a single hypercube of simulated leading edges produced from combinations of seven parameters. These parameters are the distance R and speed V, central latitude θ_0 and latitude width $\Delta\theta$, central longitude ϕ_0 and longitude width $\Delta\phi$, and the distortion parameter ρ. The new hypercube contains over 10 times the number of leading edges as in Version 1, 4021920 leading edges while the combination of the two cubes from Version 1 contains 311640 edges [*Tappin and Howard*, 2009]. The model code was also rewritten to improve its performance and speed.

[22] The heliocentric distance r of the part of the CME at an angle ψ_0 from the central axis is given by

$$\frac{r}{r_{\text{cent}}} = 1 - \rho\left(\frac{1}{\cos\psi_0} - 1\right), \tag{1}$$

where ρ is the distortion parameter and r_{cent} is the heliocentric distance of the CME along the central axis. The values of ρ range from −2.5 to +3.0 in increments of 0.5.

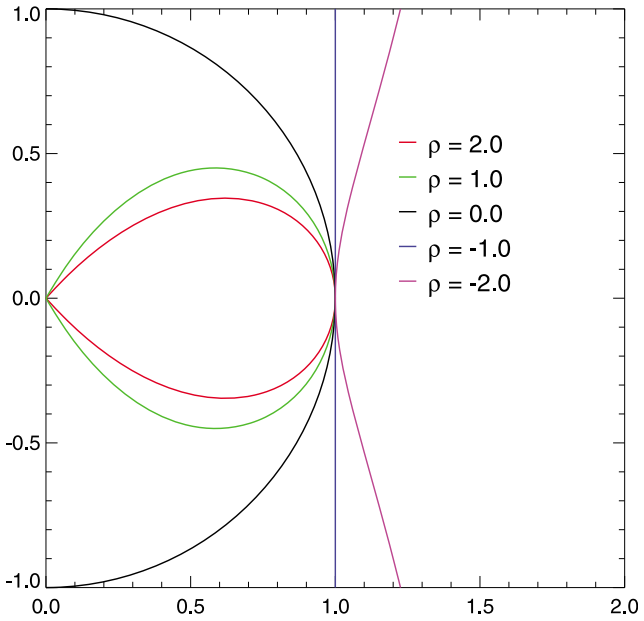

Figure 1. A selection of cross-sections from the new leading edges for varying values of distortion parameter ρ. The Sun is at the origin, the units are in AU and the CMEs are shown when their noses are at 1 AU. As shown the cases where $\rho \geq 1.0$ are the bubble cases, $\rho = 0.0$ is the spherical shell case, $\rho = -1.0$ is the "flat" CME case, and concave out CMEs occur when $\rho < -1.0$. Version 2 of the TH Model considers ρ values ranging from −2.5 to +3.0 in increments of 0.5.

Figure 1 shows a diagram of some of the new structures for different values of ρ. For example, when $\rho = 0.0$ we have the simple spherical shell (as in Version 1), when $\rho = 1.0$ we have an approximate bubble, and when $\rho = -1.0$ the CME is a flat plane. So, we accommodate for possible CMEs that are concave-out by considering ρ values less than −1.0.

[23] Finally, the means by which the model incorporates STEREO data have been modified. Accommodating for STEREO proved difficult due to the relatively large differences in radial distance of each STEREO spacecraft compared with the Earth. This was significant enough to require separate grids for each observer [*Howard and Tappin*, 2009b]. In Version 1, separate leading edge hypercubes were developed for each different observer, so there was a dedicated hypercube when observing from SMEI and one for each STEREO spacecraft. This approach has two drawbacks.

[24] 1. The heliocentric distance of the observer can only be expressed with limited accuracy (one radial step or 0.05 AU).

[25] 2. With the increased number of synthetic sky maps that must be generated to create the edge database for the bent shell models, computation time becomes prohibitive.

[26] Therefore we have opted to simply scale the radii by the heliocentric distance of the observing spacecraft. This is not an exact solution as the densities will not be strictly accurate, but the effect of this on the leading edge location is very small for the less than 10% distance changes for SMEI and the STEREO HIs.

3.3. Determining Probability of Impact and Arrival Time

[27] Once the TH Model has performed the leading edge reconstruction of the CME, we may use the converged properties to determine how it interacts with objects in the heliosphere. The structural parameters can be used to determine whether it will impact any point in space, and its kinematic properties can determine its arrival time and speed at that point. Hence we can use the model to identify the arrival time at any spacecraft, planet, or body in the heliosphere provided the location of the body is determined relative to the CME. The model can also determine what part of the CME (nose, flanks, etc) is likely to impact the body, or by how much the CME missed the body if no part of it passes through. Finally, we can estimate the speed with which the CME impacted the body, by extending the CME converged speed parameters to the projected arrival time.

[28] With knowledge of the location of the Earth relative to the CME, we can hence determine the impact likelihood and time and speed of arrival of the CME there.

3.3.1. Will an Impact With the Earth Occur?

[29] Let us first consider the conditions required for the CME to impact the Earth. A cross-section of the CME in longitude/latitude coordinates is an ellipse with equation

$$\frac{(\phi - \phi_0)^2}{\Delta\phi^2} + \frac{(\theta - \theta_0)^2}{\Delta\theta^2} = 1, \tag{2}$$

where the independent variables ϕ and θ represent the longitude and latitude variation across the CME respectively, ϕ_0 and $\Delta\phi$ are the central longitude and longitude width of the CME, and θ_0 and $\Delta\theta$ are the central latitude and latitude width, as mentioned previously. Figure 2 shows the geometry of this ellipse in the case where the CME impacts the Earth. Note that the Earth (the origin in this coordinate system) is located within the area of the ellipse. Note also that the axes of the ellipse are always aligned with the latitude and longitude axes. We considered adding a tilt angle to the ellipse axes but concluded that an additional free parameter would be prohibitive for both the accuracy of convergence and runtime of the model. One may expect the effects of tilt angle to become more significant for cross-sections with larger ellipticity.

[30] Two conditions must be satisfied for this intersection to occur. First, the latitudinal extent of the CME must be such that it crosses the ecliptic plane (the ϕ-axis in Figure 2). That is,

$$|\theta_0| \leq \Delta\theta. \tag{3}$$

Given this condition we can determine the longitudes at which the CME intersects the ecliptic plane by solving

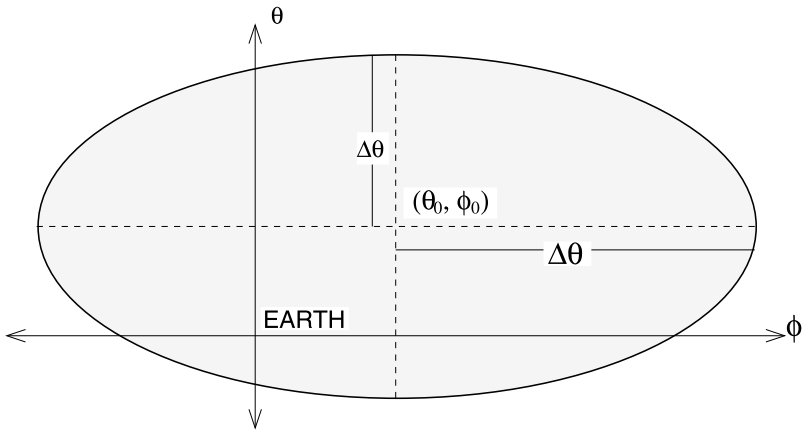

Figure 2. Diagram of the cross-section of a CME leading edge, as determined by the TH Model, for the case where the CME impacts the Earth. This is shown in spherical coordinates of longitude ϕ and latitude θ. Indicated are the location of the Earth at the origin along with the longitude and latitude sizes of the CME ($\Delta\phi$ and $\Delta\theta$ respectively) and the coordinates of the CME center (θ_0,ϕ_0). An impact with the Earth is known because the origin of the coordinate system lies within the area of the ellipse.

Equation (2) for ϕ with θ set to zero. So the ellipse crosses the Φ-axis at

$$\phi = \phi_0 \pm \sqrt{\Delta\phi^2\left(1 - \left(\frac{\theta_0}{\Delta\theta}\right)^2\right)}. \quad (4)$$

For impact with the Earth the ϕ-intercepts must be on either side of the origin. So,

$$|\phi_0| < \sqrt{\Delta\phi^2\left(1 - \left(\frac{\theta_0}{\Delta\theta}\right)^2\right)}. \quad (5)$$

Hence, for any CME simulated with the TH Model, an impact with the Earth will occur if Equations (3) and (5) are simultaneously satisfied.

3.3.2. Time of Arrival

[31] If an impact has been predicted, we can determine the time of arrival of the CME at the Earth. This is not as simple as with the spherical shell approximation, which arrives at 1 AU simultaneously across the entire structure. Here we must identify the part of the CME which impacts the Earth and when that particular part arrives there. A CME with a curvature greater than the spherical shell, for example, would have its flanks arrive at 1 AU later than its nose, so the location of the Earth relative to the CME structure is important.

[32] Equation (1) describes the radial distance r of any point on the simulated CME for a given ψ_0, where ψ_0 is the angle between the center of the structure and the point. This distance is a factor of the actual central radius of the CME. The angle from the center of the structure to the ecliptic plane can be determined from

$$\cos\psi_0 = \cos\phi_0 \cos\theta_0, \quad (6)$$

which, when substituted into Equation (1) reveals

$$\frac{r}{r_{\text{cent}}} = 1 - \rho\left(\frac{1}{\cos\phi_0 \cos\theta_0} - 1\right). \quad (7)$$

As all the parameters in the TH Model are derived for the central point, we must determine the actual distance of the central point when the Earth-impacting part of the CME arrives at 1 AU. The distance of the center of the CME, r_{cent}, is then simply given by r_{cent} = (1 AU)/r.

[33] To determine the time at which the center of the CME reaches r_{cent} we take advantage of the initial conditions of the model, which include both a distance R_0 and a time t_0. We also have a linear speed V derived from the model which is assumed to be constant. So the time t_1 at which the CME arrives at the Earth is

$$t_1 = t_0 + \frac{r_{\text{cent}} - R_0}{V}. \quad (8)$$

3.3.3. By How Much Did It Miss the Earth?

[34] If the modeled CME is found to not impact the Earth (i.e. one or both of Equations (3) and (5) are not satisfied), a helpful parameter is the angular distance by which the CME missed. This is found by identifying the closest approach of the CME and applying spherical geometry, taking into consideration the simulated structure of the CME itself. The miss distance is useful in space weather forecasting as it can be used to estimate the likelihood of impact. If the CME missed by a large distance then this likelihood is very low. If, however, it missed by only a small distance, then there is a chance that an impact may occur, with the chances decreasing with increasing miss distance. Future work on a large survey of events will assign a prob-

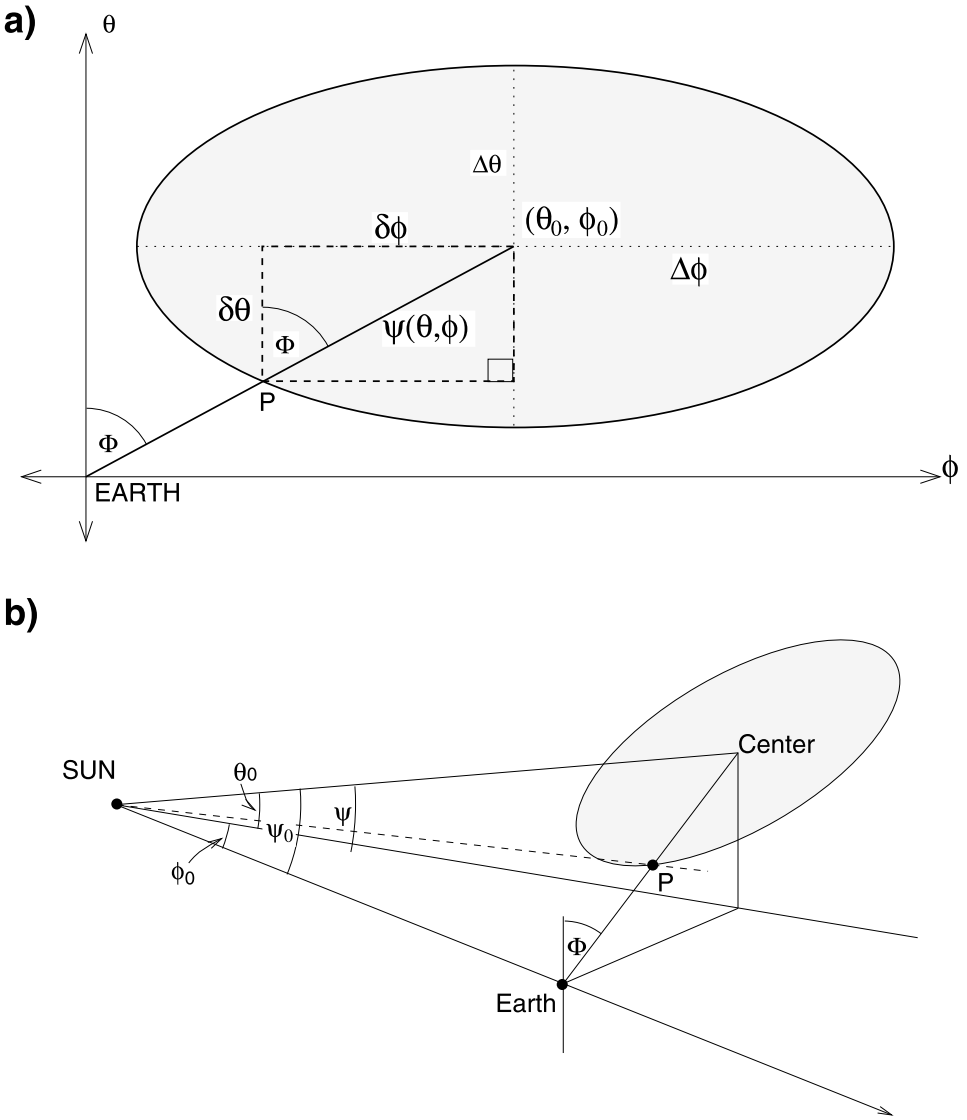

Figure 3. (a) Modeled CME cross-section for the case where the CME misses the Earth, given with the same parameters and coordinate system as in Figure 2. Here the origin is located outside the area of the ellipse, showing that it has missed the Earth. The point of closest approach is indicated (P) along with the longitudinal and latitudinal distance of P from the center of the CME ($\delta\phi$ and $\delta\theta$ respectively). The angular separation between the CME center and the point of closest approach is shown as ψ, which in this coordinate system is a function of ϕ and θ. (b) Cartesian representation of the CME relative to the location of the Sun and the Earth. Along with the angular separation of the center of the CME to the ecliptic plane (ψ_0), the central longitude and latitude (ϕ_0,θ_0) are indicated. Also shown is the angle Φ which is the position angle of the CME, from the Sun-Earth line.

ability for the miss distance and this is part of the underway validation process beyond the scope of the present work.

[35] In the case of the CME that misses the Earth consider the diagram shown in Figure 3a. The ellipse has the same structure and is in the same coordinate system as in Figure 2 except that this time the origin (the location of the Earth) does not lie inside the ellipse. The center of the ellipse is located at a position angle Φ which is also shown. This representation in heliospheric space (i.e. relative to the Sun-Earth line) is shown in Figure 3b. The latitude θ and longitude ϕ of the center of the CME are indicated along with the angular separation between the center of the CME and the Sun-Earth line ψ_0. Noting that the dis-

tance to the center of the CME is measured relative to the actual distance later we can easily show that

$$\cos\Phi = \frac{\sin\phi_0}{\sin\psi_0}. \quad (9)$$

[36] The point of closest approach, P, is shown in Figure 3a and is located at longitudinal and latitudinal separations of $\delta\theta$ and $\delta\phi$ from the center. So if we let θ and ϕ be the coordinates of P then Equation (2) becomes

$$\frac{\delta\phi^2}{\Delta\phi^2} + \frac{\delta\theta^2}{\Delta\theta^2} = 1. \quad (10)$$

Also, from the geometry shown in Figure 3a,

$$\tan\Phi = \frac{\delta\phi}{\delta\theta}, \quad (11)$$

which upon substitution into Equation (10) reveals

$$\delta\phi = \frac{1}{\sqrt{\frac{1}{\Delta\phi^2} + \frac{1}{\Delta\theta^2\tan^2\Phi}}}. \quad (12)$$

Then

$$\delta\theta = \frac{1}{\tan\Phi\sqrt{\frac{1}{\Delta\phi^2} + \frac{1}{\Delta\theta^2\tan^2\Phi}}}. \quad (13)$$

Equations (12) and (13) describe the angular separation components between the center of the CME and the point of closest approach. The actual angular separation ψ is therefore determined from

$$\cos\psi = \cos(\delta\phi)\,\cos(\delta\theta). \quad (14)$$

The closest approach is then simply the difference between ψ_0 based on the central latitude and longitude (Equation (1)) and ψ. This is measured in units of angle along the arc containing ψ. The time of closest approach may be determined in the same manner as the impact case.

4. Mock Forecast

[37] The objective of the present paper is to demonstrate the potential utility of the TH Model for space weather forecasting, specifically the arrival time and speed of an Earth-directed coronal mass ejection. To this end, we have selected three events that have been investigated in previous studies and pretend we are observing them for the first time. Each event first appears as a halo (or partial halo) coronal mass ejection in white light coronagraphs, from the Large Angle Spectroscopic Coronagraph (LASCO) on board SOHO and (for one event) the CORs on board STEREO. Speed measurements from LASCO allow us to estimate the time at which we may expect to first observe each event in the heliospheric imagers, and we look for the CME in their data from that time. Once the CME appears, measurements accumulate until we have sufficient to perform the TH Model to a successful conversion (typically around 4 or 5 SMEI images or a combination of SMEI and HI images). The TH Model is then run with these measurements, adding new measurements and additional re-runs of the model as further orbits are received. Stage 1 is run a number of times in order to minimize statistically insignificant convergences which occasionally arise in the genetic algorithm. In all cases the times required for each stage are logged, along with an allowance for an appropriate latency between actual observation and the appearance of the images on the computer. The procedure is detailed in Section 4.2.

4.1. Events

[38] Three events were selected for this initial study. The first was an Earth-directed geoeffective coronal mass ejection that was detected late in May 2003 [*Tappin et al.*, 2004]. There were two coronal mass ejections associated with this event: The first was launched on 26 May and the second on 28 May. The second was considerably faster than the first. There were two shocks detected by the ACE spacecraft near the Earth a few days later. The first was a weak shock which arrived at 11:55UT on 29 May and a much stronger shock arrived at 18:30UT on the same day. Later still on that day at around 21:00UT a geomagnetic storm was initiated with the occurrence of a sudden commencement. The storm achieved a maximum K_p of 8+ and minimum Dst of −131. We believe it is the second shock that is associated with the sudden commencement.

[39] The second event was a geoeffective CME detected in early December 2004 [*Howard et al.*, 2006a]. The CME associated with this event erupted at the beginning of 3 December (00:24UT) and an interplanetary shock arrived at ACE on 5 December at 06:56UT. Less than an hour later, at 07:45UT a sudden commencement indicated the onset of the geomagnetic storm (K_{pmax} = 4+, Dst_{min} = −58).

[40] The third event occurred in mid-November 2007 and was observed by a large range of instruments, including LASCO, the SECCHI and PLASTIC instruments on STEREO and ACE. It was associated with a shock observed by ACE and STEREO-B, but there was something unusual about the event in STEREO-A. *Howard and Tappin* [2009b] reported that it was likely to be a combination of a CME and a corotating interaction region (CIR), with the former component impacting ACE and STEREO-B and the latter arriving at STEREO-A. The shock arrived at STEREO-B and ACE on 13:50UT and 17:15UT on 19 November, and weaker shocks arrived at STEREO-A at 21:30UT and 23:45UT on 20 November. A small geomagnetic storm was associated with this event, starting around 18:11UT on 20 November.

[41] The first and second event occurred before the launch of STEREO, and so only LASCO data were used in the CME identification and SMEI data used for the TH Model. For the third event, we used LASCO, the CORs and HI-1s to identify and predict the arrival in SMEI and the HI-2s, and a combination of SMEI and HI-2 leading edge measurements were used for the TH Model. The

mock forecast for Event 1 was run using Version 1 of the model and for Event 2 we used Version 2. For Event 3 we used Version 2 with the STEREO modification. This is not the same as *Howard and Tappin* [2009b], who used Version 1 for their model convergence.

4.2. Procedure

[42] Because of the different versions used for each event, a slightly different procedure was used for each mock forecast.

4.2.1. Event 1 (Staged on 2 March 2009)

[43] The procedure for Event 1 is as follows.

[44] 1. The halo (Earth-directed) coronal mass ejection is observed by the coronagraphs on board SOHO.

[45] 2. Confirm the event is Earth-directed by checking for other solar "surface" phenomena (such as flares, erupting filaments, coronal dimming etc).

[46] 3. A data latency is allowed for the transfer of the data from spacecraft to the ground and for the creation of the images to be measured. We have assumed a latency of four hours for LASCO and SMEI. This is based on careful evaluation and testing of the SMEI transfer times, allowing for maximum delay in data transfer and post processing timing with current computer systems.

[47] 4. Height-time measurements are made from the leading edge of the coronal mass ejection and a constant speed estimated by assigning a least squares linear fit through the height-time measurements, and making use of the Point-P approximation.

[48] 5. Based on the constant speed assumption, the arrival time of the CME in the field of view of the innermost camera of SMEI is predicted. This is around 20° elongation, or around 75 solar radii. Using the same speed, an assumption of the CME arrival at 1 AU can also be estimated.

[49] 6. Starting a little before the estimated arrival time in SMEI, images are observed as they become available for the appearance of the CME. We include the four hour data latency.

[50] 7. Once the CME has been confirmed in SMEI, a sufficient number of images are allowed to emerge so that enough measurements are available to feed to the TH Model. We begin the first prediction when four clear images of the CME have appeared (a clear image is one where a measurable leading edge is defined).

[51] 8. Measure the leading edges of the four CME images, including the data gaps.

[52] 9. Feed the measurements to the TH Model and run Stage 1. In the Log, we have recorded the time required for each run of the TH Model.

[53] 10. When the model is complete it will produce a converging set of parameters along with an indication of the "goodness" of fit of these parameters.

[54] 11. One of these parameters is speed, from which an estimate of arrival time at 1 AU can be made.

[55] 12. As new images appear, repeat steps 7–10 by adding the new measurements to the database to be fed to the TH Model. Because the model does not require any order for the measurements to be entered, this allows additional measurements on previous images to be made as well. This is helpful as parts of the CME (e.g. in different parts of the sky) may have been missed in previous images which may become clearer when compared with later images.

[56] 13. Each new image allows a new execution of the TH Model, producing a new prediction each time.

[57] 14. (Optional) When sufficient images are available (at least 7 or 8), then we can run the Stage 2 part of the TH Model, to gain some idea of how the speed is varying with time.

4.2.2. Event 2 (Staged on 15 and 18 May 2009)

[58] For Event 2 we used Version 2 of the TH Model. We did not run Stage 2, but instead ran Stage 1 five times for each measurement and identified the median, maximum and minimum. This is at Step 9 in the previous section.

[59] The new version also includes an automatic time of arrival determination tool (Section 3.3). This calculates whether or not the modeled CME passes the Earth and its time of arrival there if it does. If it does not it provides a time of closest approach to the Earth of the event and a measurement of by how much it missed the Earth. This is at Step 11.

4.2.3. Event 3 (Staged on 8 October 2009)

[60] The main difference with Event 3 is that for this event data from the COR and HI instruments on STEREO were available. Here we assumed the same data latency of four hours for the CORs, but only two hours for HI. We have reduced the latency for the HIs because the HI team has already demonstrated short-latency by making the beacon images available in near-real time (C. J. Eyles, private communication, 2009).

[61] As Event 3 could be tracked continuously in STEREO-B from the CORs to HI-1 and then HI-2, there was no need to estimate the arrival time in SMEI using forward projection of coronagraph speed measurements. As explained by *Howard and Tappin* [2009b], it was necessary to await observation by all three heliospheric imagers (HI-2A, HI-2B and SMEI) before a reliable convergence of the TH Model (and hence a reliable prediction) could be produced. There was a data gap in STEREO-A from 18 November around 01:00UT to 19 November around 03:00UT, and so the first image in HI-2A in which the event appears is on 02:59UT. This then became the first time at which we begin looking for the event in SMEI, meaning that once the next SMEI image (02:10–03:52UT) was recorded on the computer we could investigate the series of images leading up to it. As it turned out, the event first appeared in SMEI in the next image (03:52–05:33UT) and confirmed in the following image, so the first prediction was made after the TH Model was performed when this image reached the computer. This resulted in a first prediction time at 13:40UT on 19 November (mock trial time), four days after launch and $4\frac{1}{2}$ hours before impact with the Earth.

[62] To demonstrate the usage of the model with desktop computers it was run for Event 3 using the computer

of the lead author, which performed at a slower rate than the high-speed computer at NSO used for Events 1 and 2. Given that the speed of the TH Model is linearly dependent on the number of images it processes and that there were a large number of HI-2B images to process, we were unable to obtain the total of five images during the 102 min between SMEI images. So we reduced the number of runs to four and then three for later runs, when even more images were needed to be processed. As shown in the Log (auxiliary material), it took around 20 min to perform a single run for the event.[1]

[63] The objective was to produce an early prediction of CME speed and arrival time at the Earth using the first few images of the CME in SMEI and HI. It is anticipated that the early prediction will be less accurate, and its accuracy will improve as more images become available. For faster events such as Event 1 or events with data gaps such as Event 3, this does not allow a large number of predictions to be made before it is too close for useful prediction. More predictions were possible for the slower fully covered Event 2.

5. Log

[64] The Log of each forecast is included as auxiliary material. The following notes are important for its interpretation.

[65] 1. Two Times: Because the timing of these events was different from the times at which the procedure was carried out, we have listed two times in the Log. The first is the actual timing of the events themselves (May 2003, December 2004 and November 2007) and the second is the time log on the day of the mock prediction (March, May and October 2009). We have recorded the time in this way so we can keep track of the time it takes to make the required measurements and run the model. Hence, the actual timing in the first column is a reflection of the time taken to make the necessary measurements. Data latency is also included in the first column.

[66] 2. Predictions (bold font): When the TH Model is complete and a prediction made, this time is highlighted by bold font. The following are listed: a) whether the model predicted an impact with the Earth (Hit) or not (No Hit); b) The modeled speed of the CME; c) The predicted arrival date and time for a Hit, or time of closest approach for a No Hit.

[67] 3. Shock Arrival and Storm Times: When the CME arrives at the in-situ spacecraft (ACE and PLASTIC) it is often preceded by a shock. This is certainly the case with the three events reported here. Hence the arrival time of the CME at ACE (at 0.99 AU) and STEREO-A (~1.05 AU) and STEREO-B (~0.95 AU) can be accurately measured. Also when the CME arrives at the Earth it begins the geomagnetic storm. The best indicator of such an occurrence is the Sudden Storm Commencement (SSC), the time of which is noted in the Log. Predictions made after this time are therefore meaningless. The times of shock arrival and geomagnetic storm onset are marked with an underlining of the text.

6. Results

[68] Figure 4 shows the results from the TH Model conversion for Event 1. Figure 4a shows a zenithal equidistant ("fisheye") SMEI image of the event on 14:08–15:50UT on 29 May with the modeled leading edge at 14:49UT superimposed. Figure 4b shows the same map of the modeled CME from which the leading edge was generated and Figure 4c shows the 3-D reconstruction of this event. The reconstruction shows an almost head-on collision of the CME with the Earth, which may account for the intensity of the resulting storm. Similar images for Events 2 and 3 have been presented in previous publications [*Tappin and Howard*, 2009; *Howard and Tappin*, 2009b] so we do not reproduce them here.

[69] The complete version of the mock forecasts, including each prediction, the time at which it was made, whether it was predicted to hit or not, and its predicted time and speed of arrival is detailed in the Log. A summary of important results is outlined in Table 2, with travel time given as the time of first appearance in the coronagraph to the arrival of the associated sudden commencement at the Earth. The average CME speed is simply the distance (1 AU) divided by the travel time, and does not accommodate for acceleration effects.

[70] To summarize, for the first event we were able to produce a prediction nine hours before the impact with the Earth, and the accuracy of this prediction was within one hour. For the second event we could produce a prediction much earlier (17 hours before impact) but the prediction was less accurate: 10 hours. For the second event the accuracy of predicted arrival time improved until the last prediction within 15 min of the actual arrival time. This prediction was made one hour before the CME shock was detected at ACE. We arrived at an accuracy within one hour, five hours before impact. For the third event the first prediction was made only $4\frac{1}{2}$ hours before impact, but all four of the predicted arrival times were within two hours. This means that in all three cases the TH Model produced predictions within two hours. We note that for Events 1 and 3 there was no direct relationship between the predicted arrival time accuracy and the time at which the prediction was made.

[71] Figure 5 (left) shows plots of predicted time of arrival vs time of prediction for the three events. This provides an indication of how the predictions change with passing time. The median and upper and lower limits for the prediction are included except for Event 1, where there was only time to run Version 1 once before the next SMEI image became available. For Event 1, the most accurate prediction is the first and predicted arrival times move away from the actual until around 17:00UT on 28 May (28.7). Accuracies then show improvement until

[1] Auxiliary materials are available in the HTML. doi:10.1029/2009SW000531.

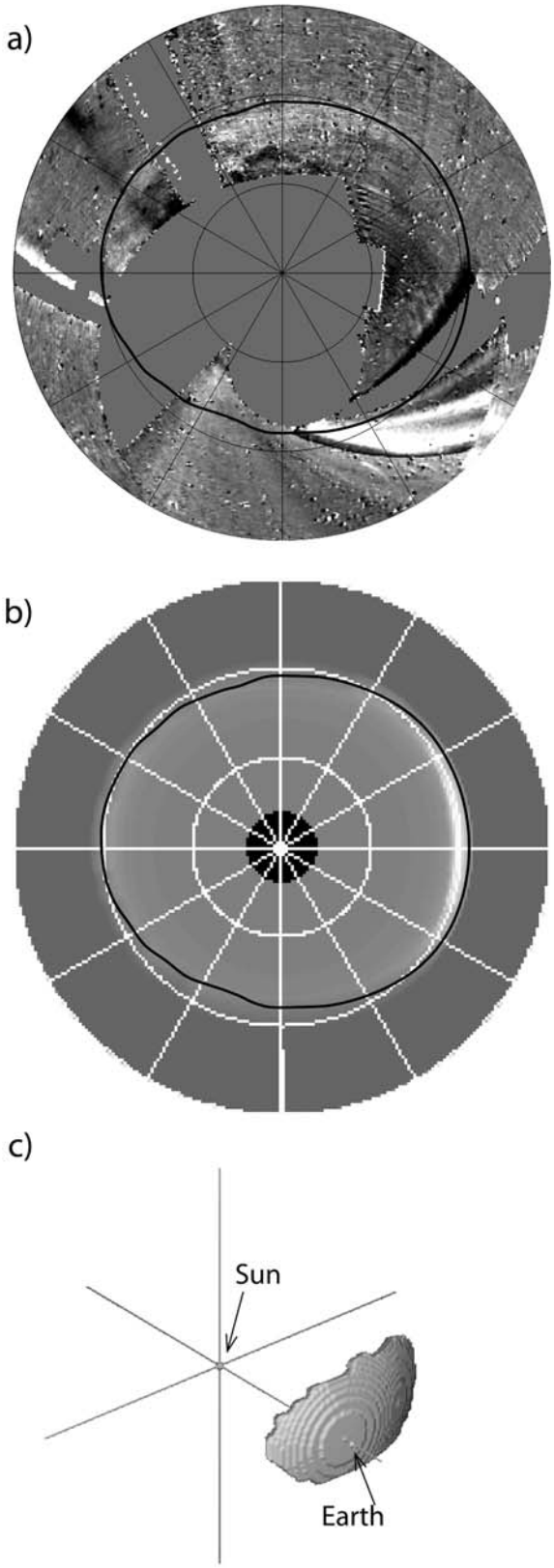

Figure 4. Images for Event 1 observed in late May 2003. (a) SMEI image from the orbit running from 14:08 to 15:50UT, with the modeled leading edge from the final forecast simulation computed at 14:59UT superposed. The projection is a "fisheye" cut off at 90° elongation. (b) Modeled image for the final simulation at R = 0.9AU (15:42UT), with the same leading edge superposed. (c) A 3-D view of the structure of final modeled disturbance, again at R = 0.9 AU. Viewed from 40°E 30°N.

impact. For Event 2, with the exception of one outlier, there is a clear tendency for the prediction to improve with increasing measurements, and for Event 3 the predictions were roughly level at around 1.5 hour difference, with the exception of the more accurate outlier. The tendency in Event 2 is what was hoped for, with an early less accurate prediction followed by successive predictions with increasing accuracy. The differences in the other events may be due to the lateness of their first predictions, but further investigation with a large number of events is needed.

[72] Figure 5 (right) shows a plot of predicted time of arrival vs elongation of the measured leading edge from the Sun (excluding Event 1). This provides an indication of how far from the Sun the CME was when we make the measurements (90° elongation ~ arrival at 1 AU for an Earthward CME).

[73] Figure 6 shows the accuracy of the speed measurements with increasing time. For Events 1 and 2 the accuracy dropped off for several predictions before improving again and there were not enough measurements to identify a trend for Event 3. For Event 1 the largest deviation was 378 km s^{-1}, for Event 2 it was 208 km s^{-1} and only 41 km s^{-1} for Event 3. It is also shown that the speed was generally overestimated for Events 2 and 3, but underestimated for Event 1. This may be due to the difference between the speed of the bulk plasma and that of the shock. If the shocked material is responsible for the observed leading edge in SMEI and the HIs, then the speed with which the material was traveling would be expected to be the shock speed, which is faster than the bulk plasma speed [e.g., *Howard and Tappin*, 2005].

7. Discussion

[74] The TH Model demonstrates the potential for early arrival time and arrival speed forecasting and with further validation could become a powerful tool for accurate high speed space weather forecasting. We are confident that accuracy can be improved with an operational version of a heliospheric imager.

[75] The mock forecasting performed with this limited number of events has shown that the model can produce early predictions up to 17 hours before impact, and this can be made earlier if a future mission can observe closer to the Sun or if the HI-1s can be incorporated. Attempts to include HI-1, however, have so far shown unreliable

Table 2. Summary of the Mock Trial Results From the Three Events[a]

	Event 1	Event 2	Event 3
Time of first appearance of CME (UT)	28 May 01:40	3 Dec 00:26	15 Nov 18:10
Time of arrival at Earth (UT)	29 May 21:00	5 Dec 07:45	19 Nov 18:11
Total travel time	1 day 19 h 20 mins	2 days 7 h 19 mins	4 days 1 min
Time of first prediction (UT)	29 May 11:50	4 Dec 15:06	19 Nov 13:40
(time after impact)	(−9 h 10 mins)	(−16 h 39 mins)	(−4 h 31 mins)
First predicted arrival time (UT)	29 May 21:31	5 Dec 21:41	19 Nov 19:35
(time after impact)	(+0 h 31 mins)	(+9 h 56 mins)	(+1 h 24 mins)
Time of last prediction (UT)	29 May 20:23	5 Dec 05:53	19 Nov 17:59
(time after impact)	(−0 h 47 mins)	(−1 h 52 mins)	(−0 h 12 mins)
Last predicted arrival time (UT)	29 May 23:49	5 Dec 07:31	19 Nov 19:55
(time after impact)	(+2 h 49 mins)	(−0 h 14 mins)	(+1 h 44 mins)
Most accurate predicted arrival time (UT)	29 May 21:31	5 Dec 07:31	19 Nov 17:51
(time after impact)	(+0 h 31 mins)	(−0 h 14 mins)	(−0 h 20 mins)
First predicted arrival speed (km s^{-1})	467	584	450
Last predicted arrival speed (km s^{-1})	675	658	471
ACE bulk plasma speed of CME (km s^{-1})	750	450	430
Average CME speed (km s^{-1})	962	753	433

[a]Times in brackets are how long after impact the measurement or prediction was made. A positive (+) value indicates a time after impact while a negative (−) time indicates before impact.

results [e.g., *Howard and Tappin*, 2009b]. Forecasts using SMEI for one event are shown to improve with time, allowing later and more accurate predictions until the CME impacts the Earth. We have also shown that predictions of accuracies within an hour of the arrival time can be made up to 12 hours before impact, and that accuracies better than 30 minutes can be achieved.

[76] Arrival speed measurements have also shown great promise, with the largest deviation for the high-speed Event 1. The reason for the variation in the speed measurements is currently unknown, but it is likely that the CME continues to accelerate or decelerate in the field of view of the heliospheric imagers. Such acceleration can be estimated using Stage 2 of the TH Model [*Tappin and Howard*, 2009; *Howard and Tappin*, 2009b] but the reliability of such estimations is currently questionable.

[77] The forecast using the combination of SMEI and STEREO data have, for one case, also shown encouraging results, with all predicted arrival times within two hours of the actual times and the most accurate speed predictions of the three cases. This validates the heliospheric image incorporation techniques of the TH Model, including the adjustment of the location of the starting point R_0.

[78] The model is currently undergoing a validation process to enable it to be used for forecasting and to be compared with existing forecasting models and methods. This validation includes a statistical survey of a number of geoeffective CMEs that have been observed by heliospheric imagers, as well as the calculation of a probability of impact based on the location of the Earth relative to the CME. We intend to eventually include automatic measurements of leading edges in the heliospheric images in order to objectify the selection and measurement process. These efforts are currently underway. From there a fixed procedure for establishing the forecast will be accomplished including arrival time and speed, probability of impact and reliability of forecast.

[79] One major restriction of the utility of the TH Model for CME forecasting is the relative late timing of the first forecast. This is due to two reasons. First, the model relies on heliospheric image data, which are not available until the CME is at least at around 20° elongation (~0.35 AU from the Sun). For SMEI, it takes a number of images before the CME can be reliably identified and then further images must be accumulated before the model will converge to a reliable solution, so it is more likely the CME will have reached 0.5 AU before we are able to run the model with any degree of confidence. Secondly, the model must await the arrival of the appropriate images at a computer in order for the leading edges to be measured. This then requires a short data latency, which is not possible with SMEI. SMEI has a long latency because of the means by which the Coriolis spacecraft transmits data to the ground, and because the raw data need to be "stitched together" into sky maps before they can be used. Here is where the STEREO spacecraft have an advantage, as they transmit beacon mode images at a much higher rate and do not require significant post-processing before its images can

Figure 5. Plots of predicted time of arrival for (a) Event 1, (b) Event 2 and (c) Event 3 vs (left) time of mock prediction and (right) leading edge elongation. The time of actual arrival is indicated by the horizontal line. For both plots for Event 2 the median, maximum and minimum predicted times are shown. Times are given as fractions of the day in December 2004, so for example for Event 2, 5.4 is 09:36UT on 5 December. The asterisk in the left plots indicates the time of the SSC.

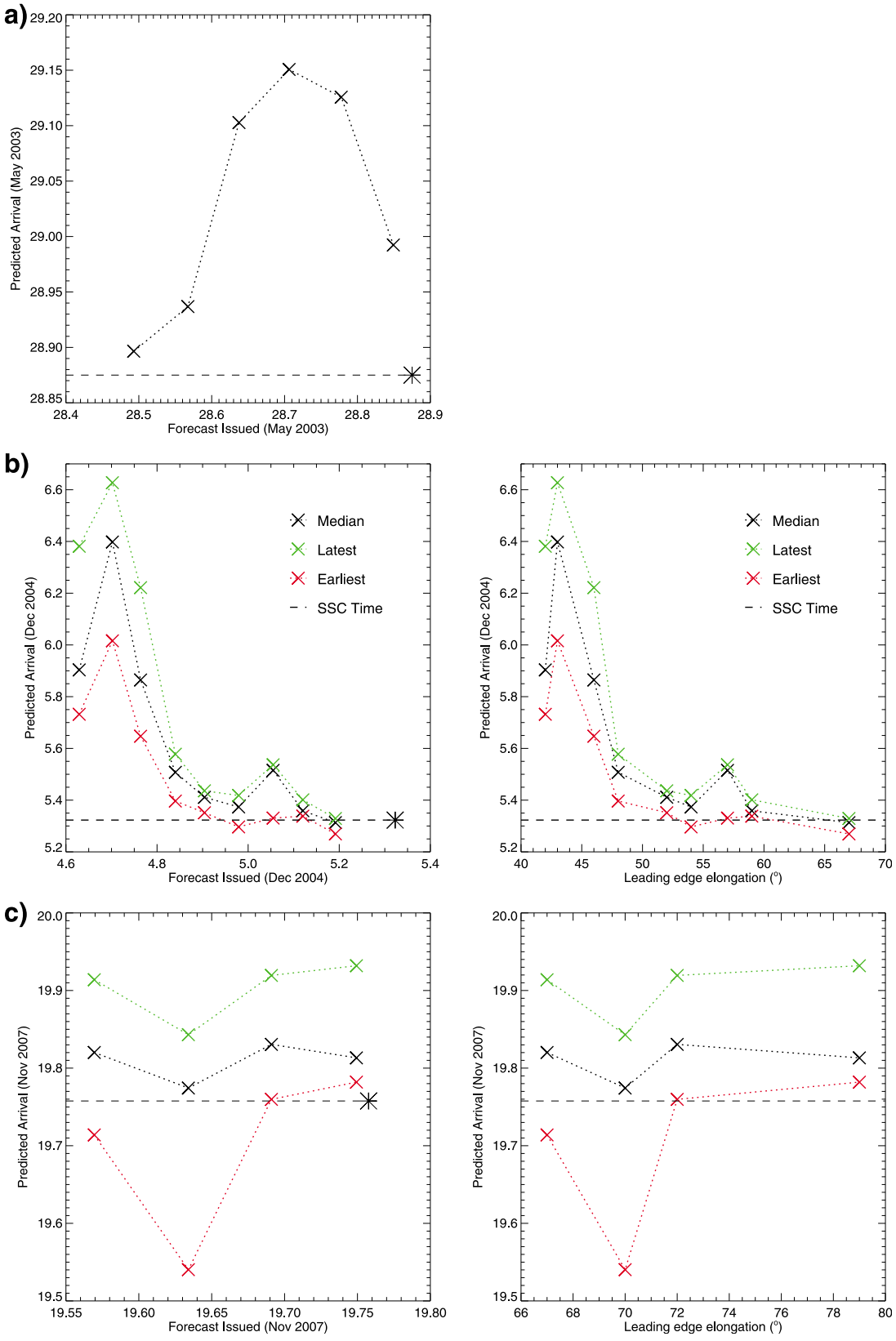
a)
Predicted Arrival (May 2003)
Forecast Issued (May 2003)
b)
Predicted Arrival (Dec 2004)
Forecast Issued (Dec 2004)
Median
Latest
Earliest
SSC Time
Leading edge elongation (°)
c)
Predicted Arrival (Nov 2007)
Forecast Issued (Nov 2007)
Leading edge elongation (°)

Figure 5

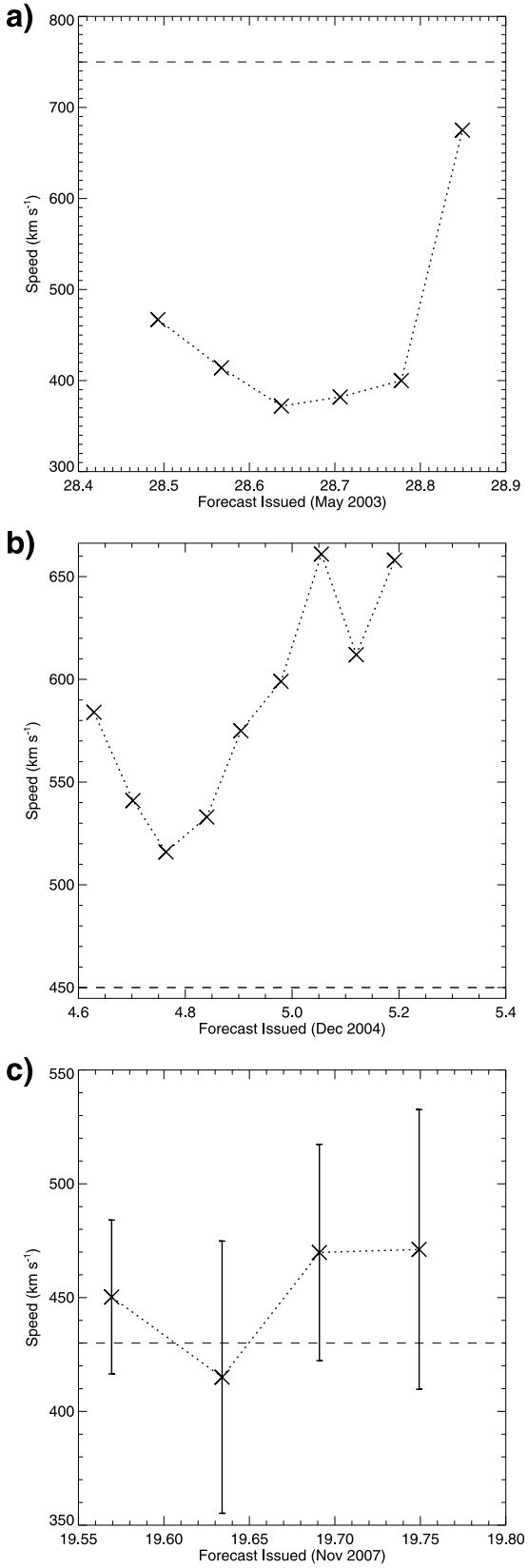

be used. As mentioned earlier, the HI team has demonstrated a capability of providing HI beacon images in near-real-time. When regarding methods to improve data latency one must consider such issues as antenna coverage needed to maintain a full stream and the downlink cycle.

7.1. CME-Based Space Weather Forecast Utility: Future Heliospheric Imager Mission

[80] The success of the TH Model for CME arrival time and speed forecasting depends entirely on the availability of heliospheric image data of sufficient quality and sky coverage to allow accurate conversions. There are currently three heliospheric imagers in operation with the capability of observing white light CMEs beyond 30° elongation: SMEI and the HI-2s. SMEI has been in operation for seven years and hot pixels have been slowly degrading the images obtained with its innermost camera (Camera 3) during its lifetime. It is likely that this camera will be unusable in the next 1–2 years. Without Camera 3 SMEI will not be able to be used for early CME detection as Earth-directed CMEs will be much closer to the Earth (0.85 AU) before they appear in its next camera (Camera 2).

[81] The STEREO spacecraft continue on their orbit about the Sun with their expanding angular separation from the Earth. They will reach the plane of the Sun around February 2011 and will become less effective at Earth-directed CME detection beyond this time. This will be because of their large distance from the Earth and the physics that allow us to observe the scattered light from the CMEs, which require backside CMEs to decrease rapidly in intensity with increasing distance from the Sun. It is important to note that no $\varepsilon > 30°$ heliospheric imager has ever observed a back-sided CME.

[82] Hence in about two years time (by around early 2012) there will be no useful heliospheric imagers available for space weather forecasting. We therefore conclude this report with an evaluation of the currently available heliospheric imagers with regard to the TH Model, and with recommendations for consideration in the design of future heliospheric imagers.

7.2. Limitations of SMEI and HI-2

[83] A key limitation to the accuracy of the TH Model is the inability to obtain full coverage of the measured CMEs. Instruments currently in operation limit this capability for reasons that differ for each instrument.

[84] For SMEI the polar orbit introduces noise from particles, auroral ovals and the South Atlantic Anomaly that obscure large parts of the SMEI field of view. Also lim-

Figure 6. Predicted speed vs time of forecast for (a) Event 1, (b) Event 2 and (c) Event 3. For Figures 6a and 6b only the speeds are shown, but for Figure 6c the standard deviations are shown as error bars. The horizontal dashed line represents the actual bulk plasma speed measured by the ACE spacecraft.

itations in thermal design causes Camera 3 (the innermost camera) to run hot, resulting in hot pixels that obscure parts of the sky map. The inner part of the field of view is blocked, resulting in late detection of the CME and the data latency is comparatively long. For HI the limited position angle range (localized only near the equator) is too restrictive for accurate reconstruction, the long exposure time results in a smearing of CME images making leading edge measurements difficult to make, and the orbit of the STEREO spacecraft are not favorable for long-term space weather monitoring.

[85] For optimum compatibility with the TH Model a future heliospheric imager would therefore need to have full position angle coverage, active CCD cooling to ensure the instrument is operating at optimum temperatures, short exposure time at any point on the image (e.g. a scanner like SMEI), and an orbit that does not pass through the polar cap or South Atlantic Anomaly (e.g. equatorial orbit or L1). If such noise can be minimized the location of the spacecraft is not important, so long as it is not too far from the Sun-Earth line. The TH Model can operate from any perspective. We would require a means to measure closer to the Sun (e.g. an additional wide-field coronagraph or full-PA version of the HI-1 instrument) and shorter data latency. Ideally the time to download and process an image should be equal to or smaller than the cadence of the instrument.

7.3. Concluding Remarks

[86] The present paper demonstrates the potential utility of the TH Model for CME-related space weather forecasting and the value of scientific and operational information obtained from heliospheric imagers. Arrival times and speeds show great promise for high-speed, highly accurate forecasting, and a complete validation is underway to assess its performance. As the model relies on heliospheric image measurements, predictions are later than other models, limiting its capability for early forecasting. It is also a phenomenological model, so cannot perform without a CME or with a CME that is not observed to have a clear leading edge. We aspire to eventually offer the TH Model as part of the collective of space weather forecasting tools, and encourage the use of heliospheric image data with existing forecasting techniques.

[87] **Acknowledgments.** SMEI was designed and constructed by a team of scientists and engineers from the Air Force Research Laboratory, the University of California at San Diego, Boston College, Boston University (US), and the University of Birmingham (UK). SOHO is a project of international cooperation between ESA and NASA. The Heliospheric Imager (HI) was developed by a collaboration including the Rutherford Appleton Laboratory and the University of Birmingham (UK), the Centre Spatial de Liége (Belgium), and the Naval Research Laboratory (US). This work is supported in part by the National Research Council Fellowship Program, funded by AFOSR contract F49620-02C-0015 and the NSF SHINE competition, award 0849916. The National Solar Observatory is operated by AURA, Inc., under cooperative agreement with the National Science Foundation. Support for S.J.T.'s work at NSO is provided by the USAF under a Memorandum of Agreement.

References

Baker, D. N., et al. (2009), *Severe Space Weather Events—Understanding Societal and Economic Impacts: A Workshop Report*, Natl. Acad. Press, Washington, D. C.

Brueckner, G. E., et al. (1995), The large angle spectroscopic coronagraph, *Sol. Phys.*, *162*, 357.

Cargill, P. J. (2004), On the aerodynamic drag force acting on interplanetary coronal mass ejections, *Sol. Phys.*, *221*, 135.

Chen, J. (1996), Theory of prominence eruption and propagation: Interplanetary consequences, *J. Geophys. Res.*, *101*, 27,499.

Davis, C. J., J. A. Davies, M. Lockwood, A. P. Rouillard, C. J. Eyles, and R. A. Harrison (2009), Stereoscopic imaging of an Earth-impacting solar coronal mass ejection: A major milestone for the STEREO mission, *Geophys. Res. Lett.*, *36*, L08102, doi:10.1029/2009GL038021.

Dungey, J. W. (1963), The structure of the exosphere or adventures in velocity space, in *Geophysics: The Earth's Environment*, edited by C. DeWitt, J. Hieblot, and A. Lebeau, p. 550, Gordon and Breach, New York.

Eyles, C. J., G. M. Simnett, M. P. Cooke, B. V. Jackson, A. Buffington, N. R. Waltham, J. M. King, P. A. Anderson, and P. E. Holladay (2003), The Solar Mass Ejection Imager (SMEI), *Sol. Phys.*, *217*, 319.

Eyles, C. J., et al. (2009), The heliospheric imagers onboard the STEREO mission, *Sol. Phys.*, *254*, 387.

Fry, C. D., W. Sun, C. S. Deehr, M. Dryer, Z. Smith, S.-I. Akasofu, M. Tokumaru, and M. Kojima (2001), Improvements to the HAF solar wind model for space weather predictions, *J. Geophys. Res.*, *106*, 20,985.

Hakamada, H., and S.-I. Akasofu (1982), Simulation of three-dimensional solar wind disturbances and resulting geomagnetic storms, *Space Sci. Rev.*, *31*, 3.

Harrison, R. A., et al. (2008), First imaging of coronal mass ejections in the heliosphere viewed from outside the Sun-Earth line, *Sol. Phys.*, *247*, 171.

Houminer, Z., and A. Hewish (1972), Long-lived sectors of enhanced density irregularities in the solar wind, *Planet. Space Sci.*, *20*, 1703.

Howard, T. A., and S. J. Tappin (2005), Statistical survey of earth-bound interplanetary shocks, associated coronal mass ejections and their space weather consequences, *Astron. Astrophys.*, *440*, 373.

Howard, T. A., and S. J. Tappin (2009a), Interplanetary coronal mass ejections observed in the heliosphere, 1. Theory, *Space Sci. Rev.*, *147*, 31.

Howard, T. A., and S. J. Tappin (2009b), Interplanetary coronal mass ejections observed in the heliosphere, 3. Physical implications, *Space Sci. Rev.*, *147*, 89.

Howard, T. A., J. C. Johnston, and D. F. Webb (2006a), Coronal mass evolution in the inner heliosphere: Geometry and speed, *Eos Trans. AGU*, *87*(52), Fall Meet. Suppl., Abstract SH32A-04.

Howard, T. A., D. F. Webb, S. J. Tappin, D. R. Mizuno, and J. C. Johnston (2006b), Tracking halo coronal mass ejections from 0–1 AU and space weather forecasting using the Solar Mass Ejection Imager (SMEI), *J. Geophys. Res.*, *111*, A04105, doi:10.1029/2005JA011349.

Hundhausen, A. J., J. T. Burkepile, and O. C. St. Cyr (1994), Speeds of coronal mass ejections: SMM observations from 1980 and 1984–1989, *J. Geophys. Res.*, *99*, 6543.

Jackson, B. V., and H. R. Froehling (1995), Three-dimensional reconstruction of a coronal mass ejection, *Astron. Astrophys.*, *299*, 885.

Jackson, B. V., A. Buffington, P. P. Hick, X. Wang, and D. Webb (2006), Preliminary three-dimensional analysis of the heliospheric response to the 28 October 2003 CME using SMEI white-light observations, *J. Geophys. Res.*, *111*, A04S91, doi:10.1029/2004JA010942.

Kahler, S. W., and D. F. Webb (2007), V arc interplanetary coronal mass ejections observed with the Solar Mass Ejection Imager, *J. Geophys. Res.*, *112*, A09103, doi:10.1029/2007JA012358.

Lugaz, N., A. Vourlidas, and I. I. Roussev (2009), Deriving the radial distances of wide coronal mass ejections from elongation measurements in the heliosphere—Application to CME-CME interaction, *Ann. Geophys.*, *27*, 3479.

Odstrcil, D., R. Riley, J. A. Linker, R. Lionello, Z. Mikic, and V. J. Pizzo (2003), 3-D simulations of ICMEs by coupled coronal and heliospheric models, in *Solar Variability as an Input to the Earth's Environment*, edited by A. Wilson, *Eur. Space Agency Spec. Publ.*, *ESA SP-535*, 541.

Smith, Z. K., and M. Dryer (1995), The interplanetary shock propagation model: A model for predicting solar-flare-caused geomagnetic sudden impulses based on the 2-1/2D MHD numerical simulation results from the Interplanetary Global Model (2D IGM), *Tech. Memo. ERL/SEL-89*, NOAA, Silver Spring, Md.

St. Cyr, O. C., et al. (2000), Properties of coronal mass ejections: SOHO LASCO observations from January 1996 to June 1998, *J. Geophys. Res.*, *105*, 18,169.

Tappin, S. J. (2006), The deceleration of an interplanetary transient from the Sun to 5 AU, *Sol. Phys.*, *233*, 233.

Tappin, S. J., and T. A. Howard (2009), Interplanetary coronal mass ejections observed in the heliosphere, 2. Model and data comparison, *Space Sci. Rev.*, *147*, 55.

Tappin, S. J., et al. (2004), Tracking a major interplanetary disturbance with SMEI, *Geophys. Res. Lett.*, *31*, L02802, doi:10.1029/2003GL018766.

Webb, D. F., et al. (2006), Solar Mass Ejection Imager (SMEI) observations of coronal mass ejections (CMEs) in the heliosphere, *J. Geophys. Res.*, *111*, A12101, doi:10.1029/2006JA011655.

Webb, D. F., T. A. Howard, C. D. Fry, T. A. Kuchar, D. R. Mizuno, J. C. Johnston, and B. V. Jackson (2009), Studying geoeffective interplanetary coronal mass ejections between the Sun and Earth: Space weather implications of Solar Mass Ejection Imager observations, *Space Weather*, *7*, S05002, doi:10.1029/2008SW000409.

Xie, H., L. Ofman, and G. Lawrence (2004), Cone model for halo CMEs: Application to space weather forecasting, *J. Geophys. Res.*, *109*, A03109, doi:10.1029/2003JA010226.

Yashiro, S., N. Gopalswamy, G. Michalek, O. C. St. Cyr, S. P. Plunkett, N. B. Rich, and R. A. Howard (2004), A catalog of white light coronal mass ejections observed by the SOHO spacecraft, *J. Geophys. Res.*, *109*, A07105, doi:10.1029/2003JA010282.

T. A. Howard, Department of Space Studies, Southwest Research Institute, 1050 Walnut St., Ste. 300, Boulder, CO 80302, USA. (howard@boulder.swri.edu)

S. J. Tappin, National Solar Observatory, Sunspot, NM 88349, USA.